

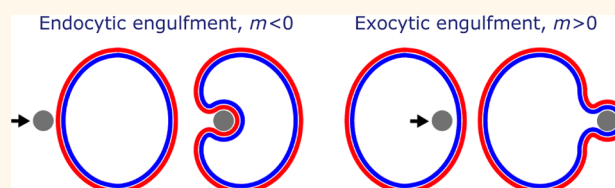
Critical Particle Sizes for the Engulfment of Nanoparticles by Membranes and Vesicles with Bilayer Asymmetry

Jaime Agudo-Canalejo and Reinhard Lipowsky*

Theory & Biosystems, Max Planck Institute of Colloids and Interfaces, 14424 Potsdam, Germany

ABSTRACT The adhesion and engulfment of nanoparticles by biomembranes is essential for many processes such as biomedical imaging, drug delivery, nanotoxicity, and viral infection. Many studies have shown that both surface chemistry, which determines the adhesive strength of the membrane—particle interactions, and particle size represent key parameters for these processes. Here, we show that

the asymmetry between the two leaflets of a bilayer membrane provides another key parameter for the engulfment of nanoparticles. The asymmetric membrane prefers to curve in a certain manner as quantitatively described by its spontaneous curvature. We derive two general relationships between particle size, adhesive strength, and spontaneous curvature that determine the instabilities of (i) the nonadhering or free state and (ii) the completely engulfed state of the particle. For model membranes such as lipid or polymer bilayers with a uniform composition, the two relationships lead to two critical particle sizes that determine four distinct engulfment regimes, both for the endocytic and for the exocytic engulfment process. For strong adhesion, the critical particle sizes are on the order of 10 nm, while they are on the order of 1000 nm for weak or ultraweak adhesion. Our theoretical results are therefore accessible to both experimental studies and computer simulations of model membranes. In order to address the more complex process of receptor-mediated endocytosis, we take the adhesion-induced segregation of membrane components into account and consider bound and unbound membrane segments that differ in their spontaneous curvatures. To model protein coats as formed during clathrin-dependent endocytosis, we focus on the case in which the bound membrane segments have a large spontaneous curvature compared to the unbound ones. We derive explicit expressions for the engulfment rate and the uptake of nanoparticles, which both depend on the particle size in a nonmonotonic manner, and provide a quantitative fit to experimental data for clathrin-dependent endocytosis of gold nanoparticles.



KEYWORDS: nanoparticles · membranes and vesicles · bilayer asymmetry · spontaneous curvature · endo- and exocytic engulfment · adhesion length · clathrin-dependent endocytosis · stability analysis · free energy minimization

The interaction of nanoparticles with biological and biomimetic membranes plays an important role in many different processes such as biomedical imaging, drug delivery, nanotoxicity, and viral infection.^{1–4} Two important steps of these processes are the adhesion of the particles to the membranes and their subsequent engulfment by these membranes, both steps being governed by the interplay of particle adhesion and membrane bending.⁵ Biomimetic model systems consisting of nanoparticles in contact with lipid^{6–10} or polymer¹¹ vesicles have been used to elucidate the particle adhesion and engulfment process experimentally. In addition, several theoretical approaches and computational methods have been applied to these model systems: energy minimization,^{5,12–16} Monte

Carlo simulations,^{17–19} and molecular dynamics simulations.^{20–24} Furthermore, the cellular uptake of nanoparticles, which requires particle engulfment as an important substep, has been intensively studied in the context of receptor-mediated endocytosis, both experimentally^{25,26} and theoretically.^{27–30}

The engulfment process depends on the strength of the attractive membrane–particle interactions, on the bending elasticity of the membranes, on the particle size, and on the geometry of the curved membranes. Experimental studies of several model systems have shown that the adhesive strength between lipid bilayers and inorganic materials can vary between 10^{-5} mN/m for ultraweak adhesion and 1 mN/m for strong adhesion.^{31–33} This range of adhesive

* Address correspondence to lipowsky@mpikg.mpg.de.

Received for review October 27, 2014 and accepted April 3, 2015.

Published online April 03, 2015
10.1021/acs.nano.5b01285

© 2015 American Chemical Society

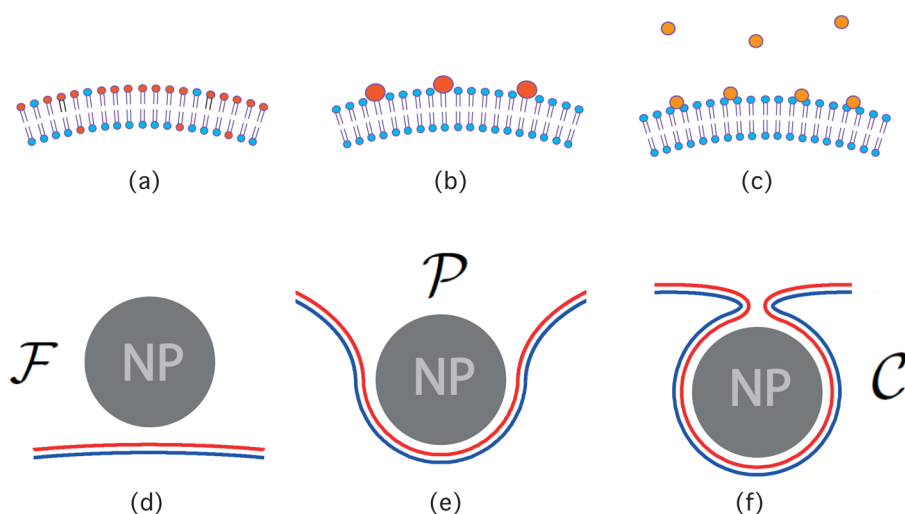


Figure 1. Engulfment of nanoparticles by asymmetric membranes: (a–c) Molecular mechanisms leading to bilayer membranes with two different leaflets: (a) compositional lipid asymmetry between the two leaflets of the bilayer; (b) asymmetric concentration of membrane-anchored molecules with a bulky headgroup such as glycolipids; and (c) asymmetric adsorption of ions or small molecules. (d–f) Different states of a spherical nanoparticle (gray, NP) in contact with an asymmetric bilayer (blue–red): (d) unbound or free state \mathcal{F} ; (e) partially engulfed state \mathcal{P} ; and (f) completely engulfed state \mathcal{C} with a narrow membrane neck that connects the adhering and unbound segments of the membrane. The lipid bilayer has a thickness of about 4 nm in all panels (a)–(f). In panels (d)–(f), the asymmetry of the bilayer is visualized by two different colors (blue and red) for the two leaflets. The nanoparticle has a radius of about 16 nm.

strengths can also be probed *via* specific receptor–ligand bonds by varying the surface density of the ligand molecules on the nanoparticles. An adhesive strength that is large compared to 1 mN/m may lead to membrane rupture. The curvature elasticity of a bilayer membrane depends on its bending rigidity, with a typical magnitude of about 10^{-19} J, and on its spontaneous curvature, which describes the asymmetries between the two leaflets of the bilayer membrane.^{34–36}

Such asymmetries can arise from a variety of molecular mechanisms; see Figure 1. First, all biological membranes have a compositional asymmetry,³⁷ and new experimental protocols have been recently developed^{38–40} by which one can mimic such an asymmetry in lipid and polymer membranes. A special case of compositional asymmetry is provided by membrane-anchored molecules with a bulky headgroup such as the glycolipids schematically shown in Figure 1b. Asymmetric membranes may also arise from the adsorption of small molecules that have different concentrations in the two aqueous phases adjacent to the membranes; see Figure 1c. Very recently, the corresponding spontaneous curvature has been determined by molecular dynamics simulations.⁴¹

In this paper, we first develop a systematic theory for the engulfment of nanoparticles by asymmetric model membranes such as lipid or polymer bilayers. These model membranes are taken to have a laterally uniform composition and, thus, a uniform spontaneous curvature. In addition, we will extend our theory to membranes with intramembrane domains induced by receptor-mediated adhesion and recruitment of coat

proteins. In the latter case, the domains are asymmetrically covered by proteins and then acquire a protein-induced spontaneous curvature. Both for uniform membranes and for membranes with intramembrane domains, we will focus on the dependence of the engulfment process on the particle size, a key parameter for the interaction of nanoparticles with membranes.^{4,25,26}

Even for the relatively simple case of nanoparticles in contact with uniform membranes, our theory predicts two critical particle sizes, R_{fr} and R_{ce} , which separate different size regimes characterized by four distinct engulfment morphologies. When the particle radius R_{pa} exceeds the critical size R_{fr} , the non-adhering or free state (Figure 1d) is unstable and the membrane starts to spread over the particle surface. When the particle radius R_{pa} is smaller than the critical size R_{ce} , the completely engulfed state (Figure 1f) is unstable and the narrow membrane neck starts to open up. In general, the critical size R_{fr} for the instability of the free state may be larger or smaller than the critical size R_{ce} for the instability of the completely engulfed state. Furthermore, we also show that the critical size R_{fr} is independent of the spontaneous curvature of the bilayer membrane, whereas the critical size R_{ce} depends strongly on this curvature, even for rather small bilayer asymmetries. The critical sizes R_{fr} and R_{ce} also depend on the origin of the nanoparticles, *i.e.*, on whether the particles originate from the exterior or interior aqueous solution. In analogy with the corresponding processes for cell membranes, we will use the terms “endocytic” and “exocytic” engulfment for particles that approach the

vesicle membranes from the exterior and interior solution, respectively.

The two critical particle sizes R_{fr} and R_{ce} are predicted to be on the order of 10 nm for strong adhesion and on the order of 1000 nm for weak or ultraweak adhesion between the nanoparticles and the lipid bilayer. This range of sizes is accessible to experimental studies with inorganic nanoparticles such as silica or glass beads as well as with organic nanoparticles based on PLGA⁴² or other polymers. In addition, the strong adhesion regime can be investigated by molecular dynamics simulations,^{20–24} whereas the weak adhesion regime can be studied by Monte Carlo^{17–19} simulations. It is also interesting to note that the typical sizes of viruses lie within the same size range between 10 and 1000 nm.

If the particles are smaller than the lower critical size, they do not adhere to the membrane and remain in their free, nonadhering state. If the particle size exceeds the upper critical size, the particles are completely engulfed by the membrane. The most interesting behavior is found for particles with an intermediate size between the two critical sizes. The intermediate size regime is characterized by partial engulfment (Figure 1e) for $R_{fr} < R_{ce}$, but exhibits bistability for $R_{fr} > R_{ce}$. In the latter case, both the free (Figure 1d) and the completely engulfed (Figure 1f) states represent metastable particle states separated by an energy barrier. For vesicles with a convex shape such as spherical or oblate vesicles, bistability is favored by negative spontaneous curvature and by endocytic engulfment, whereas partial engulfment is favored by positive spontaneous curvature and by exocytic engulfment.

In order to address the more complex process of receptor-mediated endocytosis, we generalize the instability relationships to nonuniform membranes arising from the particle-induced segregation of membrane components. The different compositions of the bound membrane segment in contact with the nanoparticle and the unbound mother membrane will, in general, lead to distinct spontaneous curvatures and bending rigidities for the two types of membrane segments. To model a membrane with a protein coat as in clathrin-dependent endocytosis, we focus on the case in which the spontaneous curvature m_{bo} of the bound segment is large compared to the spontaneous curvature m of the mother membrane. As a result, we find that nanoparticles are completely engulfed if they have an intermediate size R_{pa} with $R_{min} < R_{pa} < R_{max}$.

We also derive an equation of motion for the contact line as it moves from the free to the completely engulfed state. The solution of this equation leads to explicit expressions for the size-dependent engulfment rate and for the uptake of nanoparticles by model membranes. Both the engulfment rate and the particle uptake are nonmonotonic functions of the particle size.

In addition, the expression for the particle uptake provides a quantitative fit to the experimental data of Chithrani *et al.*,^{25,26} who studied the clathrin-dependent endocytosis of gold nanoparticles.

Our paper is organized as follows. First, we explain the basic geometry of endocytic and exocytic engulfment and how these two processes are affected by the sign of the spontaneous curvature. Second, we identify the relevant parameters of vesicle–particle systems and show that real systems can be characterized by a certain adhesion length, which varies in different systems between 10 nm and a couple of micrometers. We then consider endocytic engulfment by spherical and oblate vesicles and study the different engulfment regimes as a function of particle size, vesicle size, and spontaneous curvature. The boundary lines between these different regimes determine the critical particle sizes, which depend both on the overall vesicle size and on the spontaneous curvature of the vesicle membrane. Next, we show that these critical sizes can be obtained, in a rather general and transparent manner, if one studies the stability of the free and completely engulfed states. The corresponding stability analysis leads to two relatively simple relationships between the particle size, the adhesion length, the spontaneous curvature, and the curvatures of the local membrane segments in contact with the free or completely engulfed particles. These two relationships are then used to derive the critical particle sizes for endocytic engulfment. The corresponding results for exocytic engulfment are described in the Supporting Information (SI). We also show how a measurement of the two critical particle sizes can be used to determine the adhesion length and the spontaneous curvature. At the end, we extend our theory to receptor-mediated adhesion and engulfment and compare our results with experimental data on clathrin-dependent endocytosis of gold nanoparticles as well as with previous theoretical studies.

RESULTS AND DISCUSSION

Endocytic and Exocytic Engulfment of Nanoparticles. The strong effect of small bilayer asymmetries on the engulfment of nanoparticles can be understood intuitively if one compares endocytic and exocytic engulfment as depicted in Figure 2. In this figure, we see bilayer membranes of closed vesicles that partition space into two aqueous compartments, an exterior and an interior one. For endocytic engulfment as depicted in Figure 2a, the particle is initially located in the exterior compartment and its engulfment leads to a membrane segment that bulges toward the interior compartment. For exocytic engulfment as in Figure 2b, the particle originates from the interior compartment and leads to an adhering membrane segment that bulges toward the exterior compartment.

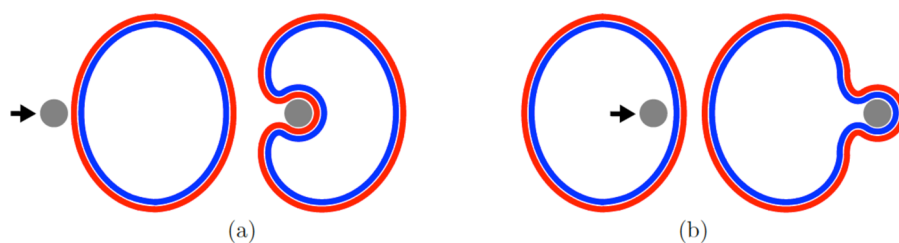


Figure 2. Nanoparticles interacting with lipid vesicles: (a) endocytic and (b) exocytic engulfment of a nanoparticle originating from the exterior and interior aqueous compartment, respectively. In both (a) and (b), the left subfigure displays the initial contact of the nanoparticle with the vesicle membrane. The bilayer membrane consists of two leaflets (blue and red) that can differ in their molecular composition; compare Figure 1. Note that the bound membrane segment around the particle bulges toward the inner (blue) leaflet in (a) and toward the outer (red) leaflet in (b). Therefore, the endocytic and exocytic processes are facilitated by bilayer asymmetries that lead to negative and positive spontaneous curvatures, $m < 0$ and $m > 0$, respectively.

In order to describe these differences in a quantitative manner, we regard the membrane as a smooth surface and consider its mean curvature M as defined by differential geometry. At any point of such a surface, the mean curvature is given by $M \equiv (1/2)(C_1 + C_2)$, where the two principal curvatures C_1 and C_2 represent the smallest and the largest curvatures of all normal surface sections through the chosen point.⁴³ It is important to note that the mean curvature can be positive or negative. The vesicles in Figure 2a and b are both convex before they interact with the nanoparticle. Likewise, after engulfment, all membrane segments of the two vesicles are still convex apart from (i) the segments adhering to the nanoparticle and (ii) the segments that form the narrow membrane necks. Membrane segments of a convex shape have a positive mean curvature $M > 0$. On the other hand, for a nanoparticle of size R_{pa} , the adhering membrane segment around the nanoparticle has the negative mean curvature $M = -1/R_{pa}$ for endocytic engulfment (Figure 2a), whereas the corresponding segment for exocytic engulfment (Figure 2b) has the positive mean curvature $M = +1/R_{pa}$.

A membrane with spontaneous curvature m tries to attain a shape for which the mean curvature M is close to m . Therefore, a *positive* spontaneous curvature supports *exocytic* engulfment as in Figure 2b, for which the adhering membrane segment has positive mean curvature, but suppresses endocytic engulfment as in Figure 2a, for which the adhering membrane segment has negative mean curvature. *Vice versa*, a *negative* spontaneous curvature supports *endocytic* and suppresses exocytic engulfment.

Relevant Parameters of Vesicle–Particle Systems. Our quantitative results are based on the free energy of the vesicle–particle systems as described in the Methods section. This free energy depends on a few geometric and material parameters: particle size, membrane area, vesicle volume, bending rigidity and spontaneous curvature of the vesicle membrane, as well as adhesive strength arising from the molecular interactions between particle and membrane. We use the membrane area A of the vesicle to define the vesicle size,

$$R_{ve} \equiv \sqrt{A/4\pi} \quad (1)$$

and take the bending rigidity κ of the membrane as the basic energy scale. In the absence of nanoparticles, the vesicle shape then depends on only two parameters,³⁵ namely, on (i) the spontaneous curvature m , which describes the asymmetry of the bilayer membrane (see Figure 1), and on (ii) the volume-to-area ratio (or reduced volume) as given by

$$v \equiv 3V/4\pi R_{ve}^3 \quad (2)$$

Note that the dimensionless quantity v satisfies $0 < v \leq 1$, where the maximal value $v = 1$ is obtained for a spherical shape. The volume-to-area ratio is controlled by the osmotic conditions: the vesicle adjusts its volume in such a way that the osmotic pressure within the interior aqueous compartment matches the osmotic pressure in the exterior aqueous compartment, apart from small differences on the order κ/R_{ve}^3 . It is also instructive to consider the special case of small osmotic pressures for which the vesicle can freely adjust its volume. Note that, in the theoretical approach used here, the membrane tension does not represent an independent parameter but plays the role of a Lagrange multiplier that is determined by the geometric and material parameters just described in order to ensure that the membrane has a certain prescribed area A ,^{35,36} see SI Text A.

The vesicle membrane is now exposed to nanoparticles that are taken to be spherical with radius R_{pa} . The intermolecular interactions between the membrane and the particles are described by the adhesive strength $|W|$, which represents the absolute value of the adhesion energy per unit area for the particle bound to the membrane.⁴⁴ A combination of the adhesive strength $|W|$ and the bending rigidity κ defines the adhesion length,

$$R_W \equiv \sqrt{2\kappa/|W|} \quad (3)$$

which we will use instead of the parameter $|W|$. Depending on the lipid composition of the bilayer membrane and on the adhesive material, the adhesion length R_W can vary between about 10 nm for strong adhesion and a few micrometers for ultraweak

TABLE 1. Five Systems Illustrating the Wide Range of Values for the Adhesion Length R_W

adhesion regime	lipid bilayer	adhesive material	κ [10^{-19} J]	$ W $ [mJ/m ²]	R_W [nm]
strong	DMPC	silica	0.8 ^d	0.5–1 ^b	13–18
strong	eggPC	glass	≈ 1	0.15 ^c	26
intermediate	DMPC	receptor–ligand	0.8 ^d	0.03 ^d	73
weak	DOPC/DOPG	coated glass	0.4 ^e	3×10^{-4e}	510
ultraweak	DOPC/DOPG	glass	0.4 ^e	10^{-5e}	2800

^a Ref 46. ^b Ref 33. ^c Ref 31. ^d Ref 45. ^e Ref 32.

adhesion, as illustrated by the examples in Table 1. In this table, we also included one example for adhesion mediated by receptor–ligand bonds as studied in ref 45, even though the surface density of the receptor and ligand molecules has not been measured in these experiments. If the ligands on the nanoparticles have the surface density ρ_{lig} and the receptor–ligand bonds have a binding free energy $|U|$ that is large compared to $k_B T$, the contribution of these bonds to the adhesive strength $|W|$ is given by $|U|\rho_{\text{lig}}$. The binding free energy $|U|$ includes both enthalpic and entropic contributions to the bond formation and, in particular, the losses of configurational entropy suffered by the receptors and ligands during the binding process as well as the entropy gained by the release of “bound” water from the two binding partners.

Thus, apart from the volume-to-area ratio v of the vesicle, the vesicle–particle systems are characterized by four different length scales: the vesicle size R_{ve} , the particle radius R_{pa} , the adhesion length R_W , and the inverse spontaneous curvature $1/m$. The vesicle size and the particle radius represent geometric parameters, whereas the adhesion length and the spontaneous curvature are material parameters. In a typical experiment, the material parameters are more difficult to vary than the geometric parameters. In order to simplify the following discussion, we will typically choose the adhesion length R_W , which is a material parameter, as the basic length scale and then measure the particle size, the vesicle size, and the spontaneous curvature in units of R_W .

As far as the spontaneous curvature is concerned, we will first focus on *small* bilayer asymmetries in the sense that the spontaneous curvature m is small compared to the inverse adhesion length $1/R_W$. As shown below, these relatively small values of the spontaneous curvatures already lead to profound changes in the behavior of the vesicle–particle systems.

Endocytic Engulfment by Spherical and Oblate Vesicles. We now consider endocytic engulfment by vesicles with a convex shape as schematically depicted in Figure 2a and regard the particle size R_{pa} as our basic control parameter. Using a variety of theoretical methods, we studied the parameter regimes for which a nanoparticle in contact with such a vesicle attains a free, partially engulfed, or completely engulfed state. We found that

these parameter regimes can be deduced from the stability of the free particle state \mathcal{F} and the completely engulfed state \mathcal{C} . The corresponding instability lines define four different engulfment regimes denoted by \mathcal{F}_{st} , \mathcal{P}_{st} , \mathcal{C}_{st} , and \mathcal{B}_{st} as shown in Figure 3 and Figure 4 for spherical and oblate vesicles. The bistable regime \mathcal{B}_{st} contains the transition line L_* at which the free and the completely engulfed state have the same free energy. The different engulfment regimes exhibit characteristic free energy landscapes $E(\phi)$ as a function of the wrapping (or spreading) angle ϕ , which determines the fraction of the membrane-covered particle surface and, thus, the contact area between membrane and particle; see Figures S1 and S2 as well as SI Text A.

For particle radii R_{pa} that are small compared to the adhesion length R_W , the nanoparticles are free and do not adhere to the membrane. In the corresponding engulfment regime \mathcal{F}_{st} , the free particle state \mathcal{F} is stable and the completely engulfed state is unstable. For particle radii R_{pa} that are large compared to the adhesion length R_W , the particle is completely engulfed by the membrane and belongs to the engulfment regime \mathcal{C}_{st} , in which the completely engulfed state \mathcal{C} is stable, whereas the free state is unstable. The most interesting behavior is found for intermediate particle radii R_{pa} that are on the order of the adhesion length R_W . For these intermediate sizes, we find two different engulfment regimes, \mathcal{B}_{st} and \mathcal{P}_{st} . The regime \mathcal{B}_{st} is characterized by bistable behavior because both the free and the completely engulfed states are (meta)stable and separated by an energy barrier; see Figure S2d–f. Finally, in the engulfment regime \mathcal{P}_{st} , the states \mathcal{F} and \mathcal{C} are both unstable, which implies that the particle attains a partially engulfed state \mathcal{P} as in Figure 1e. The defining properties of the four engulfment regimes are summarized in Table 2.

The boundaries between the four engulfment regimes are provided by the instability lines L_{fr} and L_{ce} of the free and completely engulfed state, which depend on the vesicle size R_{ve} and on the spontaneous curvature m . Indeed, inspection of Figure 3 and Figure 4 shows that negative spontaneous curvatures lead to the bistable engulfment regime \mathcal{B}_{st} for intermediate particle sizes, whereas positive spontaneous curvatures favor the regime \mathcal{P}_{st} with partially engulfed states. Furthermore, as we increase the vesicle size R_{ve} , the bistable regime \mathcal{B}_{st} shrinks, whereas the partially engulfed regime \mathcal{P}_{st} expands.

Within the latter regime, the contact area between the membrane and the particle changes in a continuous manner as we vary the particle size R_{pa} . Thus, in the regime \mathcal{P}_{st} , the contact area increases continuously from a vanishingly small value at the instability line L_{fr} up to the total surface area of the particle at the instability line L_{ce} . In contrast, when we probe the bistable regime \mathcal{B}_{st} , the contact area changes abruptly or discontinuously as the particle size R_{pa} is varied.

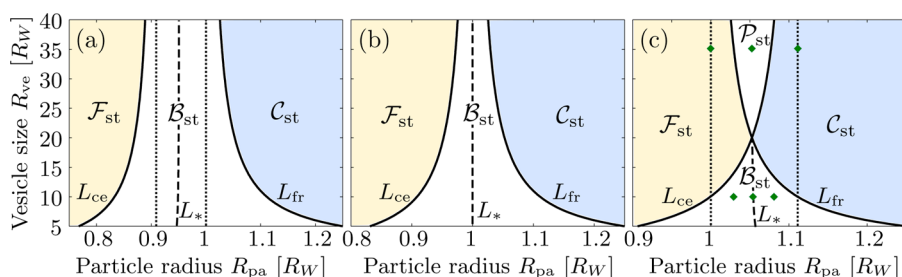


Figure 3. Different engulfment regimes \mathcal{F}_{st} (yellow), \mathcal{C}_{st} (blue), \mathcal{B}_{st} (white), and \mathcal{P}_{st} (white) for the endocytosis of a nanoparticle with radius R_{pa} by a spherical vesicle of size R_{ve} . The vesicle has a fixed membrane area and an adjustable volume. The three panels (a–c) correspond to the three values $m = -0.05/R_W$, 0 , and $+0.05/R_W$ for the spontaneous curvature m . The different regimes are defined by the two instability lines L_{fr} and L_{ce} for the free and the completely engulfed state. The asymptotes of the two instability lines for large R_{ve} are indicated by vertical dotted lines. The bistable regimes \mathcal{B}_{st} contain the transition lines L_* (dashed) at which the free and completely engulfed states coexist. For panel (c) with $m = 0.05/R_W$, the two instability lines L_{fr} and L_{ce} intersect. Close to the intersection point, the system is “multicritical” and reacts sensitively to small changes in both particle and vesicle size. The six diamonds (green) in panel (c) correspond to the free energy landscapes in Figure S2.

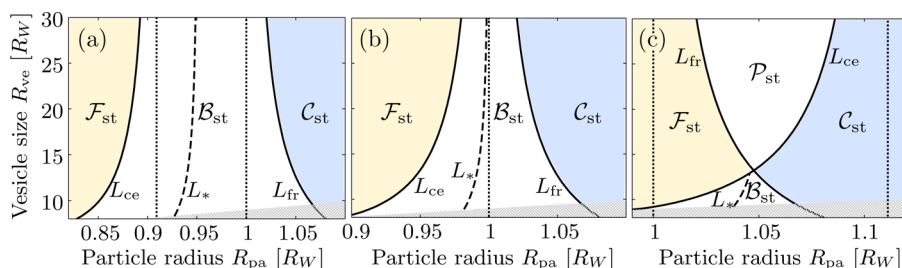


Figure 4. Different engulfment regimes for the endocytosis of a nanoparticle at the pole of an oblate vesicle with volume-to-area ratio $v = 0.98$. The three panels (a)–(c) correspond to the three values $m = -0.05/R_W$, 0 , and $+0.05/R_W$ of the spontaneous curvature. The two instability lines L_{fr} and L_{ce} , the transition line L_* , and the four engulfment regimes \mathcal{F}_{st} , \mathcal{P}_{st} , \mathcal{C}_{st} , and \mathcal{B}_{st} have the same meaning as in Figure 3. The vertical dotted lines again indicate the asymptotes of the instability lines for large R_{ve} , with L_{fr} approaching $R_{pa}/R_W = 1$ in all three cases. For panel (c), with $m = 0.05/R_W$, the intersection point of the two instability lines again leads to “multicritical” behavior. The shaded area (grey) close to the x-axis indicates the size regime in which the vesicle becomes too small to accommodate the completely engulfed particle.

TABLE 2. Four Engulfment Regimes \mathcal{F}_{st} , \mathcal{C}_{st} , \mathcal{B}_{st} , and \mathcal{P}_{st} As Defined via the (In)Stability of the Free State \mathcal{F} (Figure 1d) and by the (In)Stability of the Completely Engulfed State \mathcal{C} (Figure 1f)

	\mathcal{F}_{st}	\mathcal{C}_{st}	\mathcal{B}_{st}	\mathcal{P}_{st}
state \mathcal{F}	stable	unstable	(meta)stable	unstable
state \mathcal{C}	unstable	stable	(meta)stable	unstable

Indeed, when we enter the bistable regime \mathcal{B}_{st} from the free regime \mathcal{F}_{st} by crossing the instability line L_{ce} in Figure 3 or Figure 4, the membrane will not spread over the particle surface because the free particle state is stable up to the transition line L_* and remains metastable between the line L_* and the instability line L_{fr} ; see Figure S2d–f. Thus, spreading will occur only when we reach the instability line L_{fr} at which the free state becomes unstable and the energy barrier between the two states vanishes. Likewise, when we enter the regime \mathcal{B}_{st} from the completely engulfed regime \mathcal{C}_{st} by crossing the instability line L_{fr} , the completely engulfed state is stable up to the transition line L_* and remains metastable until we reach the instability line L_{ce} , where the energy barrier for neck opening vanishes.

For the examples shown in Figure 3 and Figure 4, the engulfment process is discontinuous for all vesicle sizes if the spontaneous curvature $m \leq 0$. For positive values of m , the engulfment process is still discontinuous for small vesicle sizes R_{ve} but continuous for large values of R_{ve} . In the latter case, the two instability lines intersect; see Figure 3c and Figure 4c. Close to the corresponding intersection points, the system exhibits “multicritical” behavior in the sense that it reacts sensitively to small changes in both particle and vesicle size.

The case with zero spontaneous curvature as illustrated in Figure 3b and Figure 4b turns out to be special: as indicated in these panels, both instability lines approach the *same* asymptotic value $R_{pa}/R_W = 1$ as the vesicle size R_{ve} becomes large. The latter behavior can be derived from explicit expressions for the instability lines L_{fr} and L_{ce} as described in the next subsections. In fact, these expressions provide two relatively simple relationships between the parameters of the vesicle–particle systems and two local curvatures of the vesicle membrane. As a consequence, these relationships allow us to explore the parameter space of these systems in a global manner.

Instability of Free State and Onset of Endocytic Engulfment.

In order to determine the instability of the free state \mathcal{F} , we compare the latter state as depicted in Figure 5a to a partially engulfed state with a small contact area as in Figure 5b. The convex membrane segment shown in Figure 5a has a positive mean curvature $M_{ms} > 0$. The latter curvature can be negative but must satisfy $M_{ms} > -1/R_{pa}$ in order to ensure that the membrane does not intersect the particle before contact. The stability limit of the free state is obtained from the requirement that the mean curvature at the attachment point is the same before and after contact, which implies that the mean curvature M_{ms} of the membrane segment before contact is equal to the contact mean curvature $M_{co} = 1/R_W - 1/R_{pa}$; see Methods section. It then follows that the instability line L_{fr} of the free state \mathcal{F} is described by

$$R_{pa} = R_{fr} \equiv \frac{1}{R_W^{-1} - M_{ms}} \quad \text{for} \\ M_{ms} < 1/R_W \quad (L_{fr}, \text{ endocytosis}) \quad (4)$$

and that the membrane segment starts to spread over the particle if

$$R_{pa} > R_{fr} \quad \text{and} \\ M_{ms} < 1/R_W \quad (\text{unstable } \mathcal{F}, \text{ endocytosis}) \quad (5)$$

For strongly curved membrane segments with a positive mean curvature M_{ms} larger than $1/R_W$, the free state \mathcal{F} is stable for all particle sizes; that is, the critical particle size $R_{fr} = \infty$. The latter situation includes the limiting case $R_{pa} = \infty$, for which the adhesive nanoparticle becomes an adhesive planar surface. Therefore, such a surface cannot bind small spherical vesicles with radius $R_{ve} = 1/M_{ms} < R_W$, in agreement with the results of ref 44.

The vesicle with an adjustable volume (Figure 3) has a spherical shape, which implies that the segment curvature M_{ms} has the constant value $M_{ms} = 1/R_{ve}$. For the oblate vesicle with fixed volume-to-area ratio $v = 0.98$ (Figure 4), the segment curvature M_{ms} at the pole depends on the spontaneous curvature m and has to be determined numerically from the shape of the free oblate vesicle, which is calculated by minimizing its free energy as described in the Methods section. The same method has been used to check and validate the instability criterion in eq 5 for a large number of different parameter values.

The onset of adhesion is related to the behavior of the free energy landscape $E(\phi)$ for small values of the wrapping angle ϕ , which is given by $E(\phi) \approx E(0) + (1/2)E''\phi^2$. As shown in the SI Text A, the second derivative E'' of the free energy with respect to ϕ at $\phi = 0$ is given by

$$E'' = 4\pi\kappa \left[-\left(\frac{R_{pa}}{R_W}\right)^2 + (1 + R_{pa} M_{ms})^2 \right] \quad (6)$$

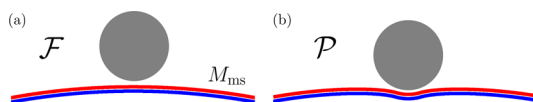


Figure 5. Onset of endocytic engulfment: (a) free state \mathcal{F} of nanoparticle (gray) and asymmetric bilayer (blue–red) compared to (b) partially engulfed state \mathcal{P} with a small contact area. The free state is unstable if the initial spreading of the bilayer membrane onto the particle leads to a gain in adhesion energy that overcompensates the increase in the membrane's bending energy. The corresponding instability criterion in eq 5 involves the mean curvature M_{ms} of the membrane segment before contact. For the convex shape shown here, the segment curvature M_{ms} is positive. In general, this curvature must be larger than $-1/R_{pa}$ to ensure that membrane and particle do not intersect each other.

This expression can be decomposed into two contributions arising from (i) the bound membrane segment in contact with the nanoparticle and (ii) the unbound membrane segment close to the contact line. For $M_{ms} = m$, the contribution from the unbound segment vanishes and E'' becomes equal to the contribution from the bound segment. The free state \mathcal{F} with $\phi = 0$ is stable and unstable if it represents a minimum and maximum of the energy landscape with $E'' > 0$ and $E'' < 0$, respectively; see Figure S2. A bit of algebra shows that the condition $E'' \leq 0$ is equivalent to the relationship $R_{pa} \geq R_{fr}$ as given by eqs 4 and 5, when we take the two constraints $R_{pa} > 0$ and $M_{ms} > -1/R_{pa}$ into account.

Instability of Completely Engulfed State and Neck Opening.

In the completely engulfed state, the nanoparticle is fully covered by the membrane, but still connected to the mother vesicle by a small membrane neck; see Figure 6a. In the coarse-grained description used here, the completely engulfed state corresponds to a limit shape with an ideal neck that is attached to the mother vesicle in a single contact point. At this contact point, the unbound membrane segment of the mother vesicle has the mean curvature M'_{ms} , which must satisfy $M'_{ms} < 1/R_{pa}$ in order to ensure that the membrane does not intersect the particle, whereas the mean curvature of the membrane segment adhering to the particle is equal to the contact mean curvature $M_{co} = 1/R_W - 1/R_{pa}$. For this limit shape, the sum of the two curvatures M_{co} and M'_{ms} is equal to twice the spontaneous curvature; see the Methods section. As a consequence, the instability line L_{ce} for the completely engulfed state \mathcal{G} is described by

$$R_{pa} = R_{ce} \equiv \frac{1}{M'_{ms} - (2m - R_W^{-1})} \quad \text{for} \\ M'_{ms} > 2m - 1/R_W \quad (L_{ce}, \text{ endocytosis}) \quad (7)$$

and the membrane neck starts to open if

$$R_{pa} < R_{ce} \quad \text{and} \\ M'_{ms} > 2m - 1/R_W \quad (\text{unstable } \mathcal{G}, \text{ endocytosis}) \quad (8)$$

If the mean curvature M'_{ms} of the unbound membrane segment is smaller than $2m - 1/R_W$, the completely

engulfed state \mathcal{C} is unstable for all particle sizes, i.e., $R_{ce} = \infty$.

The vesicle with an adjustable volume (Figure 3) still attains a spherical shape after complete engulfment of the nanoparticle, which implies that the local curvature M'_{ms} has the constant value $M'_{ms} = 1/(R_{ve}^2 - R_{pa}^2)^{1/2}$. For the oblate vesicle with $v = 0.98$ (Figure 4), the curvature M'_{ms} of the membrane segment at the pole has to be determined numerically from the shape of the mother vesicle, which is again calculated by minimizing its free energy; see the Methods section. The same method has been used to check and validate the instability criterion as given by eq 8 for a large number of different parameter values.

Critical Particle Sizes for Endocytic Engulfment. As illustrated by the examples in Figure 3 and Figure 4, the critical particle sizes can be deduced from the instability lines L_{fr} and L_{ce} for the free and completely engulfed particle states. These two lines intersect for $m = (1/2)(M_{ms} + M'_{ms})$ as in Figure 3c and Figure 4c because the two instability relations $M_{co} = M_{ms}$ and $M_{co} + M'_{ms} = 2m$ become identical in this case. Therefore, depending on the relative size of the spontaneous curvature m and the segment curvatures M_{ms} and M'_{ms} , the lower and upper critical sizes are equal to the radii R_{fr} and R_{ce} ; see Table 3.

The expressions for the instability lines and the critical particle sizes become particularly transparent in the limit of weakly curved membrane segments with

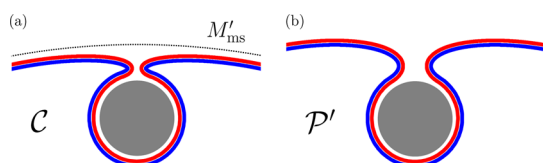


Figure 6. Opening of membrane neck for endocytic engulfment: (a) completely engulfed state \mathcal{C} of nanoparticle (gray) and asymmetric bilayer (blue–red) compared to (b) partially engulfed state \mathcal{P}' , for which the neck has been opened up. The completely engulfed state is unstable if the opening of the neck leads to a decrease in the membrane's bending energy that overcompensates the loss in adhesion energy. The corresponding instability criterion as described by eq 8 involves the mean curvature M'_{ms} of the weakly curved membrane segment (dotted line) of the mother vesicle. For a convex segment as shown here, the segment curvature M'_{ms} is positive. In general, this curvature must be smaller than $1/R_{pa}$ to ensure that the unbound and bound membrane segments do not intersect each other.

TABLE 3. Critical Particle Sizes for Endocytic Engulfment As Obtained from eqs 4–8

range of spontaneous curvature m	intermediate size regime	engulfment process	lower critical size	upper critical size
$m > (1/2)(M_{ms} + M'_{ms})$	partial \mathcal{P}_{st}	continuous	R_{fr}	R_{ce}
$m < (1/2)(M_{ms} + M'_{ms})$	bistable \mathcal{B}_{st}	discontinuous	R_{ce}	R_{fr}

small curvatures M_{ms} and M'_{ms} . More precisely, we will now assume that these segment curvatures are small both compared to the inverse particle size $1/R_{pa}$ and compared to the inverse adhesion length $1/R_W$. These requirements are certainly fulfilled for the shapes of large GUVs and for adhesion lengths R_W between about 10 and 500 nm, which covers the strong and weak adhesion regime; see Table 1. In addition, the limit of small segment curvatures M_{ms} and M'_{ms} also applies to the membrane segments that are typically studied by molecular dynamics simulations with periodic boundary conditions.^{21–23,41}

If we set the segment curvatures M_{ms} and M'_{ms} equal to zero, we obtain the simple expressions $R_{fr} = R_W$ and $R_{ce} = R_W/(1 - 2mR_W)$ for the critical particle sizes. The corresponding engulfment regimes are displayed in Figure 7b. This diagram is universal in the sense that it does not depend on the vesicle shape, which becomes irrelevant in the limit of large R_{ve} . Therefore, as we increase the vesicle size R_{ve} , we approach the engulfment regimes in Figure 7b both for spherical vesicles with adjustable volume (Figure 3) and for oblate vesicles with a certain fixed volume-to-area ratio v (Figure 4). Indeed, comparison of Figure 3a with Figure 4a, which both apply to negative spontaneous curvature $m = -0.05/R_W$, shows that the instability lines L_{ce} and L_{fr} have the same asymptotic values $R_{pa}/R_W = 0.909$ and $R_{pa}/R_W = 1$, corresponding to the vertical dotted lines in these figures. These asymptotic values are indicated in Figure 7b by the two open diamonds for $m = -0.05/R_W$. Likewise, the other open diamonds in Figure 7b correspond to the identical asymptotes in Figure 3b and Figure 4b as well as in Figure 3c and Figure 4c. The open diamond with the coordinates $R_{pa}/R_W = 1$ and $m = 0$ in Figure 7b is special because it represents the “multicritical” intersection point of the two instability lines at which all four engulfment regimes meet.

The engulfment diagram in Figure 7b is obtained for flat membrane segments with $M_{ms} = M'_{ms} = 0$. This diagram undergoes small changes if we consider small but finite values of the local membrane curvatures M_{ms} and M'_{ms} as illustrated in Figure 7a and c. These changes depend primarily on the sign of the curvature sum $M_{ms} + M'_{ms}$, which determines the intersection point for the two instability lines.

Instability Relations and Critical Sizes for Exocytic Engulfment. The instability relations for exocytic engulfment differ from those for endocytic engulfment because the expression for the contact mean curvature M_{co} is different; see eq 22 in the Methods section. The modified instability relations lead to changes in the critical particle radii and the engulfment regimes as described in the SI Text B. The Supporting Information also contains (i) Figure S3, which displays the regimes of exocytic engulfment for weakly curved mother

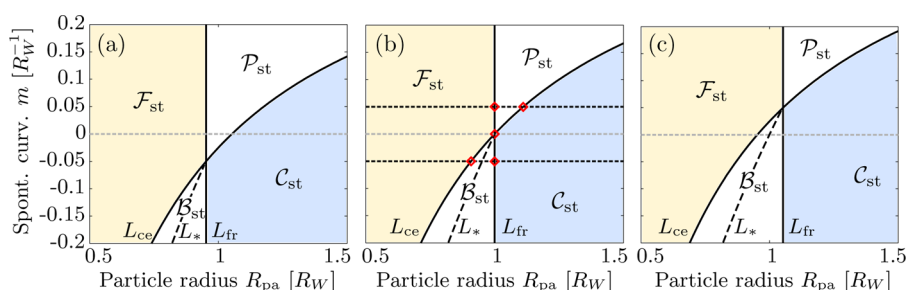


Figure 7. Endocytic engulfment of nanoparticles for weakly curved mother membranes: different engulfment regimes \mathcal{F}_{st} , \mathcal{B}_{st} , \mathcal{C}_{st} , and \mathcal{P}_{st} as a function of particle size R_{pa} and spontaneous curvature m , both measured in units of the adhesion length R_W . (a) Concave membrane segments with negative curvatures $M_{ms} = M'_{ms} = -0.05/R_W$; (b) flat segments with vanishing curvatures $M_{ms} = M'_{ms} = 0$; and (c) convex segments with positive curvatures $M_{ms} = M'_{ms} = +0.05/R_W$. The two instability lines L_{fr} and L_{ce} determine the critical particle sizes R_{fr} and R_{ce} via eqs 4 and 7. The bistable regimes \mathcal{B}_{st} contain the transition lines L^* (dashed), at which the free and completely engulfed states coexist. All four engulfment regimes meet at the “multicritical” intersection points of the two instability lines where $m = (1/2)(M_{ms} + M'_{ms})$. The five open diamonds (red) in panel (b) correspond to the asymptotes of the instability lines L_{fr} and L_{ce} for finite vesicle sizes R_{ve} , as indicated by the vertical dotted lines in Figure 3 and Figure 4.

membranes, and (ii) a detailed comparison between the latter figure and Figure 7 for the endocytic process.

Experimental and Computational Studies of Critical Particle Sizes. Inspection of the engulfment diagrams in Figures 3, 4, and 7 as well as Figure S3 shows that the critical particle sizes are always on the order of the adhesion length R_W . More precisely, for the relatively small spontaneous curvatures m studied here, the nanoparticles probe the intermediate engulfment regimes \mathcal{P}_{st} and \mathcal{B}_{st} when the particle size varies in the interval between $0.5R_W$ and $1.5R_W$. For the intermediate engulfment regime \mathcal{P}_{st} , both critical sizes R_{fr} and R_{ce} are accessible to experiment as long as we can distinguish partially from completely engulfed states. For the ultraweak adhesion regime with an adhesion length of a few micrometers (Table 1, fifth row), these different states should be accessible to conventional optical microscopy. For the strong adhesion regime with an adhesion length on the order of 10–30 nm (Table 1, first and second row), the partially and completely engulfed states could be distinguished by cryoelectron microscopy.^{2,9}

The two critical radii are also accessible to computer simulations. Indeed, both Monte Carlo^{17–19} and molecular dynamics^{20–24} simulations have been recently used to study the interactions of nanoparticles with membranes. Nanoparticles with a radius of up to 50 nm can be investigated by coarse-grained molecular dynamics, which can thus be utilized to probe the strong adhesion regime. The weak adhesion regime, on the other hand, can be elucidated via Monte Carlo simulations, by which one can study much larger particles. In the simulations, one can even probe the stability of the free and completely engulfed state directly by applying external forces to the particles.

Now, assume that we observed, in experimental studies or computer simulations, the engulfment regime \mathcal{P}_{st} for the endocytic process and that we measured the two critical sizes R_{fr} and R_{ce} . From the

microscopy images or the simulation snapshots, we would also be able to obtain the two segment curvatures M_{ms} and M'_{ms} . We can then use the explicit expressions for the instability lines to deduce the adhesion length R_W and the spontaneous curvature m from the critical particle sizes. As a result, we obtain the relationships

$$R_W = \frac{R_{fr}}{1 + R_{fr}M_{ms}} \quad (\text{cont endocytosis}) \quad (9)$$

for the adhesion length R_W and

$$m = \frac{1}{2} \left[\frac{1}{R_{fr}} - \frac{1}{R_{ce}} + M_{ms} + M'_{ms} \right] \quad (\text{cont endocytosis}) \quad (10)$$

for the spontaneous curvature m .

If the intermediate size regime for the endocytic process belongs to the bistable regime \mathcal{B}_{st} , the experimental observation of the two critical sizes is more difficult. Indeed, when we add nanoparticles to the exterior solution, the free state of the particles remains metastable up to the upper critical size and will then undergo an abrupt transition, as a function of particle size, to the completely engulfed state. Thus, for a bistable intermediate regime, we can still measure the upper critical size and, thus, the adhesion length R_W but not the lower critical size, which is necessary to determine the spontaneous curvature. However, if the endocytic process is discontinuous, the exocytic process is continuous as explained in the SI Text B. Therefore, we can then deduce the material parameters from the radii as determined from the exocytic process for the same vesicle–particle system; see eqs S18 and S19.

RECEPTOR-MEDIATED ADHESION AND ENGULFMENT

Particle-Induced Segregation of Membrane Components. In the previous sections, we considered model membranes with a laterally uniform composition and, thus,

a laterally uniform spontaneous curvature m . If the membrane contains several molecular components, these components will typically experience different interactions with the particle surface. As a consequence, the composition of the bound membrane segment can differ significantly from the composition of the unbound membrane. One example is provided by charged particles and oppositely charged lipid molecules; another example by membrane-anchored receptors or “stickers” that interact with the particle *via* specific receptor–ligand bonds. Both the oppositely charged lipids and the receptors will be enriched (or “recruited”) in the bound segments and depleted in the unbound segments.⁴⁷ The actual concentrations in the two segments are determined by the partitioning of the receptor molecules between the two membrane segments, a partitioning that depends on the affinities or binding free energies of the different components with the particle surface and on the size of the two membrane segments. In equilibrium, these concentrations follow from the requirement that each membrane component has the same chemical potential in the two membrane segments. One major contribution to these chemical potentials comes from the translational entropy of the membrane components. For receptor-mediated endocytosis, these dependencies have been studied in ref 27 using a kinetic model for the diffusing receptors and in ref 30 based on the statistical thermodynamics of many interacting receptors and nanoparticles.

Because of their distinct compositions, the two membrane segments can also differ in their fluid–elastic properties. Thus, we will now consider bound membrane segments that have a spontaneous curvature m_{bo} and a bending rigidity κ_{bo} , while the unbound membrane is still characterized by the spontaneous curvature m and the bending rigidity κ . We will again assume that the spontaneous curvature m is relatively small but will allow large values for the spontaneous membrane curvature m_{bo} of the bound membrane segment in order to model a protein coat as formed in clathrin-dependent endocytosis. Furthermore, the membrane–particle interactions involve, in general, both nonspecific (hydrophobic, van der Waals, or electrostatic) and specific interactions mediated by membrane-anchored receptors.⁴⁸ Both types of molecular interactions will be described by the adhesive strength $|W|$.

The loss of conformational entropy by the receptor–ligand bonds can also be included in $|W|$ *via* the binding free energy U of each bond. If the binding enthalpy of a receptor–ligand bond is $|H|$, the binding free energy of the bond can be estimated by $|U| = |H| - k_B T \ln(\rho_{lig}/\rho_0)$,²⁷ where ρ_{lig} and ρ_0 represent the ligand density on the particle surface and the concentration of receptors on the membrane surface before contact with the particle, respectively. The contribution of the

ligand–receptor bonds to the adhesive strength $|W|$ is then given by $|U|\rho_{lig}$ as mentioned previously.

The combined bending and adhesion free energy of such a nonuniform membrane is equal to the free energy of a uniform membrane with bending rigidity κ and spontaneous curvature m provided we replace the molecular adhesive strength $|W|$ by the effective adhesive strength

$$W_{\text{eff}} = |W| + \frac{2\kappa}{R_{\text{pa}}^2} (1 \pm R_{\text{pa}}m)^2 - \frac{2\kappa_{\text{bo}}}{R_{\text{pa}}^2} (1 \pm R_{\text{pa}}m_{\text{bo}})^2 \quad (11)$$

arising from the difference between the elastic parameters of the unbound and the bound membrane segment where the plus and minus signs apply to endo- and exocytosis, respectively. Because of this parameter mapping, the instability relations for the nonuniform membrane can be directly obtained from the previously discussed relations for uniform membranes. In the following, we will again focus on the endocytic case.

Engulfment Regimes Controlled by Bound Membrane Segment. The instabilities of the free state \mathcal{F} and of the completely engulfed state \mathcal{G} are again described by the relationships $M_{\text{co}} \geq M_{\text{ms}}$ and $M_{\text{co}} + M'_{\text{ms}} \leq 2m$ as before, but the contact mean curvature M_{co} now has the form

$$M_{\text{co}} = \sqrt{\frac{W_{\text{eff}}(R_{\text{pa}})}{2\kappa}} - \frac{1}{R_{\text{pa}}} \quad (\text{endocytosis}) \quad (12)$$

where the notation $W_{\text{eff}}(R_{\text{pa}})$ emphasizes the R_{pa} dependence of the effective adhesive strength W_{eff} as given by eq 11. Because W_{eff} depends quadratically on the particle size R_{pa} , the instability relations $M_{\text{co}} \geq M_{\text{ms}}$ and $M_{\text{co}} + M'_{\text{ms}} \leq 2m$ are no longer linear in R_{pa} . The instability lines L_{fr} and L_{ce} again follow from the instability relations $M_{\text{co}} = M_{\text{ms}}$ and $M_{\text{co}} + M'_{\text{ms}} = 2m$. As in the case of uniform membranes, these two relations are identical for $m = (1/2)(M_{\text{ms}} + M'_{\text{ms}})$, which implies that the two instability lines L_{fr} and L_{ce} are also identical in this case.

We now focus on the case of weakly curved mother membranes for which $|M_{\text{ms}}|$ and $|M'_{\text{ms}}|$ as well as $|m|$ are much smaller than $1/R_{\text{pa}}$. For the limiting case $M_{\text{ms}} = M'_{\text{ms}} = m = 0$, the two instability relations become identical to $M_{\text{co}} = 0$ or

$$\left[\frac{R_{\text{pa}}^2 |W|}{2\kappa} + 1 - \frac{\kappa_{\text{bo}}}{\kappa} (1 + R_{\text{pa}}m_{\text{bo}})^2 \right]^{1/2} = 1 \quad (13)$$

This relation leads to two engulfment regimes, $\mathcal{F}_{\text{st}}^<$ and $\mathcal{F}_{\text{st}}^>$, in which the free state \mathcal{F} is stable and the completely engulfed state \mathcal{G} is unstable; see Figure 8a. As shown in this figure, these two regimes are separated by an intermediate regime \mathcal{G}_{st} in which the free state is unstable and the completely engulfed state is

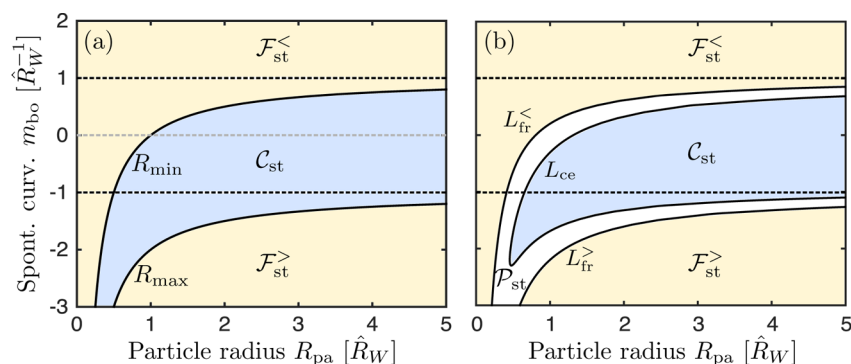


Figure 8. Engulfment regimes for weakly curved mother membranes as a function of particle radius R_{pa} and spontaneous curvature m_{bo} of the bound membrane segment in contact with the nanoparticle. Both quantities are given in units of the modified adhesion length \hat{R}_W defined in eq 16. (a) Engulfment regimes for $M_{ms} = M'_{ms} = m$ that apply to both $m = 0$ and $m \neq 0$: the regime \mathcal{C}_{st} (blue) of completely engulfed particle states is located between the two regimes $\mathcal{F}_{st}^<$ and $\mathcal{F}_{st}^>$ (yellow), both of which exhibit free particle states. For parameter values within the regime \mathcal{C}_{st} , the membrane spreads over the whole particle surface. The two boundary lines $R_{pa} = R_{min}(m_{bo})$ and $R_{pa} = R_{max}(m_{bo})$ are given by eqs 14 and 15; (b) small deviations $M_{ms} - m$ and/or $m - M'_{ms}$ lead to a “broadening” of the boundary lines as illustrated here for $M_{ms} = M'_{ms} = 0$ and $m = 0.2/\hat{R}_W$. The two boundary lines split up into separate instability lines L_{fr} and L_{ce} , which enclose a narrow boundary regime (white) around the regime \mathcal{C}_{st} . In this example, the boundary regime represents a partial engulfment regime \mathcal{P}_{st} .

stable. The boundary lines between the three engulfment regimes are given by

$$R_{pa} = R_{min} \equiv \frac{1}{\hat{R}_W^{-1} - m_{bo}} \quad \text{for } m_{bo} < +1/\hat{R}_W \quad (14)$$

and

$$R_{pa} = R_{max} \equiv \frac{1}{|m_{bo}| - \hat{R}_W^{-1}} \quad \text{for } m_{bo} < -1/\hat{R}_W \quad (15)$$

with the modified adhesion length

$$\hat{R}_W \equiv \sqrt{2\kappa_{bo}/|W|} = R_W \sqrt{\kappa_{bo}/\kappa} \quad (16)$$

It turns out that essentially the same solution applies to the more general case with $M_{ms} = M'_{ms} = m \neq 0$, for which the two instability relations become identical to $M_{co} = m$. In the latter case, the two boundary lines are truncated at $m_{bo} = (1/\hat{R}_W) - |m|$ and $m_{bo} = -(1/\hat{R}_W) - |m|$, respectively, reflecting the condition that membrane and particle surface are not allowed to intersect each other but the expressions for R_{min} and R_{max} as given by eqs 14 and 15 remain unchanged.

An expansion of the instability relations $M_{co} = M_{ms}$ and $M_{co} + M'_{ms} = 2m$ around the special case $M_{ms} = M'_{ms} = m$ leads to correction terms that are proportional to $M_{ms} - m$ and $m - M'_{ms}$, respectively. If we take these correction terms into account, the boundary lines $R_{pa} = R_{min}$ and $R_{pa} = R_{max}$ “broaden” and split up into two separate instability lines, L_{fr} and L_{ce} , that enclose a narrow boundary regime around the regime \mathcal{C}_{st} of complete engulfment. This split-up is illustrated in Figure 8b for $M_{ms} = M'_{ms} = 0$ and $m = 0.2/\hat{R}_W$. In general, such a split-up occurs as soon as $M_{ms} + M'_{ms} \neq 2m$, i.e., as soon as the segment curvatures do not match the spontaneous curvature of the mother membrane, and the resulting intermediate size regime may be a partial engulfment regime \mathcal{P}_{st} and/or a bistable regime \mathcal{B}_{st} .

Kinetics of Membrane Spreading and Particle Engulfment.

The spreading of the membrane over the particle surface proceeds *via* the displacement of the contact line. As described in the SI Text C, the contact line experiences two forces, a thermodynamic driving force and a frictional force. The thermodynamic driving force is proportional to the gradient $dE(\phi)/d\phi$ of the free energy landscape $E(\phi)$, where the wrapping angle ϕ varies from $\phi = 0$ for the free particle state to $\phi = \pi$ for the completely engulfed state.

Balancing the thermodynamic driving force with the frictional force, we obtain the equation of motion

$$\sin(\phi) \frac{d\phi}{dt} = \frac{1}{2\pi\eta_{eff}R_{pa}^3} \frac{dE(\phi)}{d\phi} \quad (17)$$

for the wrapping angle ϕ as a function of time t , which involves the effective viscosity η_{eff} . Using this equation of motion with the initial condition $\phi(t = 0) = 0$ corresponding to the free particle state \mathcal{F} , we can determine the engulfment time $t_{\mathcal{F}}$ that the membrane needs to spread over the whole particle surface and to attain the completely engulfed state \mathcal{C} within the regime \mathcal{C}_{st} in Figure 8. This time follows from the implicit equation $\phi(t = t_{\mathcal{F}}) = \pi$.

As shown in the SI Text C, the gradient $dE(\phi)/d\phi$ becomes particularly simple in the limit of small particle sizes with $R_{pa} \ll R_{ve}$. Indeed, this gradient is then determined by the contribution from the bound membrane segment alone and can be calculated in closed form; see eq S31. As a consequence, the wrapping velocity $d\phi/dt$ becomes constant and the implicit equation $\phi(t = t_{\mathcal{F}}) = \pi$ leads to the size-dependent engulfment rate

$$\omega_{\mathcal{F}} = \frac{1}{t_{\mathcal{F}}} = \frac{f(R_{pa}/\hat{R}_W)}{t_0} \quad \text{in regime } \mathcal{C}_{st} \quad (18)$$

with the time scale $t_0 \equiv \pi\eta_{eff}\hat{R}_W^3/(2\kappa_{bo})$ and the dimensionless function

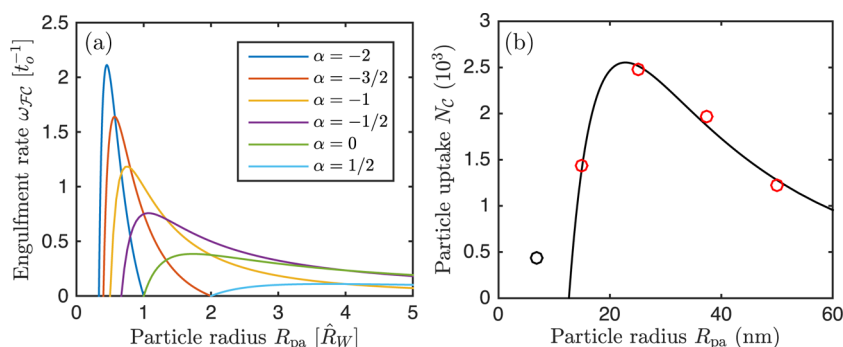


Figure 9. (a) Size dependence of engulfment rate $\omega_{\mathcal{F}c}$ in units of $1/t_0$ as given by eq 18 for different values of the reduced spontaneous curvature $\alpha = R_W m_{bo}$ of the bound membrane segment and (b) size dependence of particle uptake as measured by Chithrani *et al.*²⁶ for clathrin-dependent endocytosis of transferrin-coated gold nanoparticles (open circles) fitted by eq 20 with $R_W = 48.6$ nm and $m_{bo} = -1/(40.0$ nm). The data point for $R_{pa} = 7$ nm (black open circle) has not been included in the fit because, for this size, the clathrin-coated vesicles were observed²⁶ to engulf more than one nanoparticle. The effective radius of the nanoparticles was increased to $R_{pa} + 9.3$ nm in order to take the size of the transferrin receptor's ectodomain⁵² into account.

$$f(x) \equiv \frac{x^2 - (1 + \alpha x)^2}{x^3} \quad \text{with} \\ x \equiv R_{pa}/\hat{R}_W \quad \text{and} \quad \alpha \equiv \hat{R}_W m_{bo} \quad (19)$$

The function $f(R_{pa}/\hat{R}_W)$ describes the size dependence of the engulfment rate as illustrated in Figure 9a. The numerator $x^2 - (1 + \alpha x)^2$ of $f(x)$ is proportional to $dE/d\phi$.

The effective viscosity η_{eff} depends on the microviscosity of the bilayer and on the molecular interactions between membrane and particle. Typical values for the bilayer's microviscosity lie in the range 0.1–1 Pa s, which corresponds to 10^2 – 10^3 times the viscosity of water.^{49,50} Using $\eta_{\text{eff}} = 1$ Pa s together with $\kappa_{bo} = 10^{-19}$ J, the time scale t_0 is equal to about 1.25 ms for $\hat{R}_W = 20$ nm (strong adhesion) and to about 20 ms for $\hat{R}_W = 50$ nm (intermediate adhesion); compare Table 1. These estimates for the time scale t_0 are consistent with both experimental⁶ and computational⁵¹ studies.

Now, consider a giant vesicle in an aqueous solution without nanoparticles and let us exchange this solution, at time $t = 0$, by an aqueous dispersion of such particles with particle concentration X_{pa} . The vesicle membrane will then start to engulf nanoparticles with the rate $\omega_{\mathcal{F}c}$. The corresponding particle uptake by the vesicle is equal to the number N_c of completely engulfed particles. This number evolves in time according to $dN_c/dt = N_{\mathcal{F}} \omega_{\mathcal{F}c}$, which depends on the number $N_{\mathcal{F}}$ of free particles adjacent to the vesicle membrane. The latter number is determined by the bulk concentration X_{par} , which will be time independent as long as the number of dispersed particles is much larger than the number of particles attached to the membrane. After a certain observation time Δt , we then obtain the particle uptake

$$N_c(\Delta t) = N_{\mathcal{F}} \Delta t \omega_{\mathcal{F}c} = N_{\mathcal{F}} \frac{\Delta t}{t_0} f(R_{pa}/\hat{R}_W) \quad (20)$$

with the function $f(x)$ as given by eq 19; compare Figure 9a.

Comparison with Clathrin-Dependent Endocytosis. In the previous subsections, we considered receptor-mediated adhesion and engulfment for lipid vesicles with multicomponent membranes containing receptor or “sticker” molecules. The same processes are also involved in the uptake of nanoparticles by eukaryotic cells, which utilize a variety of different endocytic pathways^{53,54} including the much studied pathway of clathrin-dependent endocytosis.^{55–57} The size dependence of the latter process has been elucidated by Chithrani *et al.*,^{25,26} who measured the uptake of gold nanoparticles by HeLa cells for different particle sizes. As a result, the cellular uptake was found to depend on the particle size in a nonmonotonic manner as displayed in Figure 9b for the case of transferrin-coated gold nanoparticles.²⁶

One generic aspect of clathrin-dependent endocytosis is that the clathrin-coated membrane represents a strongly asymmetric membrane domain with receptor–ligand binding on its outer (exoplasmic) face and a thick protein coat consisting of adaptor proteins such as AP-2 and clathrin triskelions on its inner (cytoplasmic) face. The associated spontaneous curvature m_{bo} can be estimated from the dimensions of the clathrin-coated vesicles that are generated by the endocytic process. For native coats from human placenta,⁵⁸ the outer diameter of the coat was found to vary between 75 and 130 nm, while the enclosed vesicle had a radius between 18 and 43 nm. Thus, the spontaneous curvature m_{bo} is expected to have a value between $-1/(18$ nm) and $-1/(43$ nm), where the negative sign reflects the endocytic process; see Figure 2a. That the membrane prefers to curve in this manner can be understood from the dense coverage of the inner (cytoplasmic) face of the cell membrane by bulky adaptor proteins such as AP-2.

As shown in Figure 9b, the size dependence of the experimental data for transferrin-coated nanoparticles²⁶ is well fitted by eq 20 with $m_{bo} = -1/(40.0$ nm),

$\hat{R}_W = 48.6$ nm, and $N_{\mathcal{F}} \Delta t / t_o = 1.85 \times 10^3$. These values were obtained using the method of least-squares applied to the four data points with $R_{pa} = 15, 25, 37,$ and 50 nm. The data point with $R_{pa} = 7$ nm was excluded from the fit because, for this small size, the clathrin-coated vesicles were observed²⁶ to engulf more than one nanoparticle. The effective radius of the nanoparticles was taken to be $R_{pa} + 9.3$ nm in order to account for the size of the transferrin receptor's ectodomain,⁵² which protrudes from the membrane by 9.3 nm and, thus, increases the local separation between the particle surface and the bilayer membrane by this amount.

The deduced value $m_{bo} = -1/(40.0$ nm) for the coat-induced curvature lies within the range of m_{bo} values as estimated from the observed dimensions of clathrin-coated vesicles. The deduced value $\hat{R}_W = 48.6$ nm for the modified adhesion length together with the bending rigidity $\kappa_{bo} = 1.17 \times 10^{-18}$ J of clathrin-coated vesicles⁵⁹ leads to the adhesive strength $|W| = 2\kappa_{bo}/\hat{R}_W^2 = 0.99$ mN/m $\approx 0.24k_B T/\text{nm}^2$. On one hand, this adhesive strength is on the same order of magnitude as attractive van der Waals interactions between colloidal particles. On the other hand, this $|W|$ value could also arise from the specific receptor–ligand interactions alone. Indeed, the bond between the transferrin receptor and the transferrin molecule has been estimated, based on atomic force microscopy measurements,⁶⁰ to be about $20k_B T \approx 8.2 \times 10^{-20}$ J. Because the lateral size of a single transferrin receptor is about 5×10 nm², a densely packed layer of transferrin receptors with one molecular bond per receptor would lead to the adhesive strength $|W| = 1.64$ mN/m $\approx 0.4k_B T/\text{nm}^2$.

The main difference between clathrin-dependent endocytosis and the engulfment of nanoparticles by lipid membranes is the characteristic time scale t_o . Indeed, for the simple spreading dynamics described in the previous subsection, this time scale was estimated to be on the order of milliseconds for lipid bilayers. In contrast, it takes between 20 and 80 s to form a clathrin-coated vesicle starting from a nascent clathrin-coated pit.^{56,57} One mechanism for this slowdown of the dynamics is provided by diffusion-limited enrichment of the receptor molecules within the contact area between membrane and nanoparticle as theoretically studied in refs 27–30. For relatively low receptor concentrations and/or for relatively large nanoparticles, it can indeed take tens of seconds for a diffusing receptor to reach the contact area. However, the clathrin-dependent pathway is used by the cells even in the absence of ligands or nanoparticles in order to constitutively internalize and recycle membrane-bound receptors such as the transferrin receptor.^{61,62} Furthermore, a recent fluorescence microscopy study on the uptake of virus capsids by feline cells revealed that the assembly of the protein

coat and the formation of the clathrin-coated vesicle takes between 30 and 70 s regardless of whether it contains a virus capsid or not.⁵⁷ Because these capsids had a diameter of 26 nm and utilized transferrin receptors for their association with the cell membrane, this intrinsic time scale for the coat assembly should also apply to the clathrin-dependent uptake of gold particles as studied by Chithrani *et al.* in refs 25 and 26. After the clathrin-coated vesicle has been formed, it pinches off from the mother membrane by cleavage of the membrane neck *via* the GTPase dynamin. This fission process takes only a few seconds and is, thus, much faster than the vesicle formation step, as revealed by fluorescence microscopy.^{56,57} As a consequence, the observed size dependence of the cellular uptake should be dominated by the size dependence of the engulfment process, which corroborates our estimate based on the engulfment rate $\omega_{\mathcal{F}}$.

Comparison with Previous Theoretical Studies. It is instructive to compare our results with two previous theoretical studies on receptor-mediated endocytosis that also obtained characteristic particle sizes. First, Gao *et al.*²⁷ studied the receptor-mediated engulfment of nanoparticles in the framework of a kinetic model that emphasized the lateral diffusion of the membrane-anchored receptors. Second, Zhang *et al.*³⁰ investigated the statistical thermodynamics of many membrane-anchored receptors interacting with many nanoparticles. Both studies identified two characteristic particle sizes, R_1 and R_2 , that separate three different size regimes. For small particle sizes, $R_{pa} < R_1$, a no-engulfment regime was found in which the bending free energy dominates and prevents the onset of adhesion. For particle sizes $R_{pa} > R_1$, a complete engulfment regime was found. These two regimes were originally identified by Lipowsky and Döbereiner in ref 5 with $R_1 = R_W = (2\kappa/|W|)^{1/2}$. In the present study, these size regimes correspond to the special case of *vanishing* spontaneous curvatures $m = m_{bo} = 0$ and flat mother membranes; see the dashed horizontal lines in Figure 7b and Figure 8a corresponding to $m = 0$ and $m_{bo} = 0$, respectively.

One important result of our study is that, in the presence of even a small bilayer asymmetry generating a small spontaneous curvature $m \neq 0$, the characteristic size $R_1 = R_W$ is replaced by an intermediate size regime in which the particles either are partially engulfed or show bistable behavior; see Figure 7b. These intermediate size regimes are bounded by the two critical particle sizes, R_{fr} and R_{ce} which emerge from the “multicritical” point with $R_{pa} = R_W$ and $m = 0$ in a continuous manner.

For $R_{pa} > R_2$, Gao *et al.*²⁷ and Zhang *et al.*³⁰ considered receptor and ligand concentrations for which complete engulfment is suppressed by a shortage of receptors. Such a constraint has not been included in our theory. As mentioned in the previous subsection,

the transferrin receptors are continuously recycled between the plasma membrane and membrane-bound organelles even in the absence of nanoparticles or ligands.^{61,62} In addition, the number of receptors per nanoparticle can be relatively small, as observed for the uptake of virus capsids by feline cells.⁵⁷ However, we have found that the particle-induced segregation of membrane components can lead to two critical particle sizes, R_{\min} and R_{\max} , even without any receptor shortage provided the bound membrane domain exhibits a large negative spontaneous curvature $m_{\text{bo}} < -1/\hat{R}_W$, as shown in Figure 8a. Furthermore, as illustrated in Figure 8b, the two critical sizes R_{\min} and R_{\max} are again replaced by intermediate size regimes with partial engulfment or bistable behavior if the sum of the local segment curvatures M_{ms} and M'_{ms} deviates from twice the spontaneous curvature m of the mother membrane.

CONCLUSIONS

In the main part of this paper, we studied nanoparticles in contact with laterally uniform model membranes and showed that the membranes' spontaneous curvature m represents a key parameter of these systems, which leads to two critical radii, R_{fr} and R_{ce} , separating four distinct engulfment regimes. For particle sizes below the lower critical radius, the particle is free and does not bind to the membrane (regime \mathcal{F}_{st}). For particle sizes above the upper critical radius, the particle is completely engulfed by the membrane (regime \mathcal{C}_{st}). For intermediate particle sizes, the particle either is partially engulfed (regime \mathcal{P}_{st}) or exhibits bistable behavior (regime \mathcal{B}_{st}). The corresponding engulfment diagrams have been determined for spherical and oblate vesicles as shown in Figure 3 and Figure 4 as well as for weakly curved membranes corresponding to the limit of large vesicles; see Figure 7 and Figure S3.

The basis length scale for the engulfment processes is provided by the adhesion length $R_W = (2\kappa/|W|)^{1/2}$, which depends on the bending rigidity κ of the lipid bilayer and on the adhesive strength $|W|$ of the attractive membrane–particle interactions. In real systems, the adhesion length can vary between about 10 nm for strong adhesion and a few micrometers for ultraweak adhesion; see Table 1. For the relatively small spontaneous curvatures studied here, the nanoparticles probe the intermediate engulfment regimes \mathcal{P}_{st} and \mathcal{B}_{st} when the particle size varies in the interval between $0.5R_W$ and $1.5R_W$. As a consequence, the two critical sizes are located within the same interval.

The engulfment of silica nanoparticles by DOPC vesicles has been recently studied by cryoelectron microscopy.⁹ Complete engulfment was found for all particle sizes with a radius above 15 nm. Thus, we conclude that this system belongs to the strong adhesion regime with an adhesion length R_W below 15 nm.

This conclusion can be directly corroborated by measuring the adhesive strength $|W|$ between DOPC bilayers and silica.

As explained in the three paragraphs before eq 9, the two critical sizes will be directly accessible to experimental observations and computer simulations if the engulfment process proceeds in a continuous manner *via* partially engulfed states. If the *endocytic* process is discontinuous, corresponding to a bistable intermediate regime, the *exocytic* process will be continuous for the same vesicle–particle system, as follows from the “mirror symmetry” of the instability relations; see SI Text B. Thus, for any vesicle–particle system, either the endocytic or the exocytic engulfment process proceeds continuously *via* partially engulfed particle states.

From the observed values of the critical radii and the local membrane curvatures, one can deduce the adhesion length R_W and the spontaneous curvature m as described by eq 9 and eq 10 for continuous endocytosis and by eq S18 and eq S19 for continuous exocytosis. Therefore, the systematic variation of the size of the nanoparticles provides a possible probe to determine the material parameters of the vesicle–particle system both experimentally and *via* simulations. Using Monte Carlo^{17–19} or molecular dynamics^{20–24} simulations, one can also directly study the bistable regime by applying external forces that push the particle over the energy barrier between the free and the completely engulfed state.

In the last part of the paper, we generalized our theory to receptor-mediated adhesion and engulfment. To model a protein coat on the membrane as assembled during clathrin-dependent endocytosis, we focused on the case in which the spontaneous curvature m_{bo} of the bound membrane segment is large compared to the spontaneous curvature m of the mother membrane. For weakly curved mother membranes, we obtain the engulfment regimes shown in Figure 8. In this case, the complete engulfment regime \mathcal{C}_{st} is “sandwiched” between two regimes $\mathcal{F}_{\text{st}}^<$ and $\mathcal{F}_{\text{st}}^>$ with free particle states and no engulfment. The boundary lines $R_{\text{pa}} = R_{\min}$ and $R_{\text{pa}} = R_{\max}$ in Figure 8a are given by the simple expressions in eqs 14 and 15.

We also derived an equation of motion for the contact line (eq 17), which describes the spreading of the membrane from the free to the completely engulfed state. The solution of this equation leads to explicit expressions for the size-dependent engulfment rate (eq 18) and for the uptake of nanoparticles (eq 20) by model membranes and vesicles. Both the engulfment rate $\omega_{\mathcal{F}}$ and the particle uptake $N_{\mathcal{G}} \propto \omega_{\mathcal{F}}$ are nonmonotonic functions of the particle size; see Figure 9. In addition, as demonstrated in Figure 9b, the expression in eq 20 for the particle uptake provides a quantitative fit to the experimental data of Chithrani *et al.*,^{25,26} who studied the

size-dependent uptake of gold nanoparticles by clathrin-dependent endocytosis.

For engulfment by model membranes with a uniform spontaneous curvature m , we focused on relatively small m values in order to demonstrate that even small asymmetries between the two leaflets of the lipid bilayer have a strong effect on the engulfment process. Our instability criteria as given by eq 5 and eq 8 for endocytic engulfment as well as by eq S15 and eq S17 for exocytic engulfment are, however, quite general and apply to large values of the spontaneous curvature as well. In the latter case, the vesicles can attain relatively complex shapes with small membrane buds and narrow membrane tubes. For simplicity, we also

focused on the behavior of a single nanoparticle in contact with the membrane. If we expose a vesicle to a solution of nanoparticles and consider the engulfment of many nanoparticles by the vesicle membrane, up to three different engulfment morphologies of the nanoparticles can be simultaneously present on the same vesicle, which then exhibits a characteristic engulfment pattern, as will be described in a subsequent paper. Our approach based on the stability of the free and completely engulfed particle states is rather general and can be extended to nonspherical shapes of the nanoparticles, to deformable particles, to chemically patterned Janus particles, and to membranes with different intramembrane domains or rafts.

METHODS

Free Energy of Vesicle–Particle System. The membrane is treated as a smooth surface with mean curvature M that varies continuously along the surface. For the well-established spontaneous curvature model,^{34–36} the bending free energy of the membrane depends on two material parameters, the bending rigidity κ and the spontaneous curvature m , and has the form

$$E_{\text{be}} = \int dA 2\kappa(M - m)^2 \quad (21)$$

where the integral runs over the whole surface area of the membrane or vesicle.

The attractive molecular interactions between membrane and nanoparticle are described by the adhesive strength, $W < 0$, which represents the adhesion free energy per unit area.⁴⁴ The total adhesion free energy is then given by $E_{\text{ad}} = -|W|A_{\text{bo}}$ where A_{bo} is the area of the membrane segment bound to the particle. The total free energy, $E = E_{\text{be}} + E_{\text{ad}}$, can be decomposed into a contribution E_{bo} from the bound membrane segment and a second contribution E_{un} from the unbound segment (or mother membrane) as described in the SI Text A. The total free energy was then minimized using the so-called shooting method as described in ref 35. The same minimization procedure was previously used to study the adhesion of vesicles to flat substrate surfaces.⁴⁴

Mean Curvature along the Contact Line. If a vesicle is in contact with a spherical nanoparticle of radius R_{pa} , the bound segment and the unbound segment of the vesicle membrane are separated by a contact line. Along this contact line, the principal curvature C_1^* of the membrane parallel to the contact line is given by $C_1^* = \mp 1/R_{\text{pa}}$, where the minus and plus signs apply to endocytic and exocytic engulfment, respectively; compare Figure 2. The second principal curvature perpendicular to the contact line follows from mechanical equilibrium along this line. Minimization of the free energy leads to the value $C_2^* = \pm((2|W|/\kappa)^{1/2} - 1/R_{\text{pa}})$, where the plus and minus signs apply to endocytic and exocytic engulfment, respectively. As a consequence, the contact mean curvature has the form

$$\begin{aligned} M_{\text{co}} &= \frac{1}{2}(C_1^* + C_2^*) = \pm \left(\sqrt{\frac{|W|}{2\kappa}} - \frac{1}{R_{\text{pa}}} \right) \\ &= \pm \left(\frac{1}{R_W} - \frac{1}{R_{\text{pa}}} \right) \end{aligned} \quad (22)$$

where the plus and minus signs again apply to endocytic and exocytic engulfment.

Neck Condition for Completely Engulfed Particle. In order to characterize the membrane neck of a completely engulfed particle, we considered vesicle shapes with a finite neck size l and studied the limit of small l . This computational approach has

been previously applied to budding of uniform membranes⁶³ and to budding of intramembrane domains.⁶⁴ In this way, we derived the ideal neck condition

$$M_{\text{co}} + M'_{\text{ms}} = 2m \quad (23)$$

between the contact mean curvature M_{co} , the segment curvature M'_{ms} of the mother vesicle (Figure 6a), and the spontaneous curvature m . The same condition can also be obtained, in a somewhat heuristic manner, from the requirement that the free energy density of the membrane as given by $2\kappa(M - m)^2$ (see eq 21) is continuous across the neck. The latter requirement leads to $(M_{\text{co}} - m)^2 = (M'_{\text{ms}} - m)^2$, which is equivalent to eq 23.

Conflict of Interest: The authors declare no competing financial interest.

Acknowledgment. This study was supported by the German Research Foundation (DFG) via the IRTG 1524.

Supporting Information Available: Technical details about (A) free energy landscapes for the engulfment process with Figures S1 and S2; (B) exocytic engulfment of nanoparticles with Figure S3; and (C) spreading dynamics and engulfment rate. Figure S1 depicts the basic geometry of the vesicle–particle system for endocytic engulfment. Figure S2 illustrates the different free energy landscapes for the engulfment process, emphasizing the landscapes for the bistable regime \mathcal{B}_{st} . Figure S3 shows the four engulfment regimes for exocytic engulfment by weakly curved membranes as a function of particle size and spontaneous curvature. This material is available free of charge via the Internet at <http://pubs.acs.org>.

REFERENCES AND NOTES

- Rodriguez, P. L.; Harada, T.; Christian, D. A.; Pantano, D. A.; Tsai, R. K.; Discher, D. E. Minimal “Self” Peptides that Inhibit Phagocytic Clearance and Enhance Delivery of Nanoparticles. *Science* **2013**, *339*, 971–975.
- Chen, K. L.; Bothun, G. D. Nanoparticles Meet Cell Membranes: Probing Nonspecific Interactions Using Model Membranes. *Environ. Sci. Technol.* **2014**, *48*, 873–880.
- Björnalm, M.; Yan, Y.; Caruso, F. Engineering and Evaluating Drug Delivery Particles in Microfluidic Devices. *J. Controlled Release* **2014**, *190*, 139–149.
- Mahmoudi, M.; Meng, J.; Xue, X.; Liang, X. J.; Rahmand, M.; Pfeiffer, C.; Hartmann, R.; Gil, P. R.; Pelaz, B.; Parak, W. J.; *et al.* Interaction of Stable Colloidal Nanoparticles with Cellular Membranes. *Biotechnol. Adv.* **2014**, *32*, 679–692.
- Lipowsky, R.; Döbereiner, H.-G. Vesicles in Contact with Nanoparticles and Colloids. *Europhys. Lett.* **1998**, *43*, 219–225.
- Dietrich, C.; Angelova, M.; Pouligny, B. Adhesion of Latex Spheres to Giant Phospholipid Vesicles: Statics and Dynamics. *J. Phys. II Fr.* **1997**, *7*, 1651–1682.

7. Koltover, I.; Rädler, J.; Safinya, C. Membrane Mediated Attraction and Ordered Aggregation of Colloidal Particles Bound to Giant Phospholipid Vesicles. *Phys. Rev. Lett.* **1999**, *82*, 1991–1994.
8. Fery, A.; Moya, S.; Puech, P.-H.; Brochard-Wyart, F.; Möhwald, H. Interaction of Polyelectrolyte Coated Beads with Phospholipid Vesicles. *C. R. Phys.* **2003**, *4*, 259–264.
9. Bihan, O. L.; Bonnafous, P.; Marak, L.; Bickel, T.; Trépout, S.; Mornet, S.; Haas, F. D.; Talbot, H.; Taveau, J.-C.; Lambert, O. Cryo-Electron Tomography of Nanoparticle Transmigration into Liposome. *J. Struct. Biol.* **2009**, *168*, 419–425.
10. Michel, R.; Plostica, T.; Abezgauz, L.; Danino, D.; Grzdzinski, M. Control of the Stability and Structure of Liposomes by Means of Nanoparticles. *Soft Matter* **2013**, *9*, 4167.
11. Jaskiewicz, K.; Larsen, A.; Schaeffel, D.; Koynov, K.; Lieberwirth, I.; Fytas, G.; Landfester, K.; Kroeger, A. Incorporation of Nanoparticles into Polymersomes: Size and Concentration Effects. *ACS Nano* **2012**, *6*, 7254–7262.
12. Deserno, M. Elastic Deformation of a Fluid Membrane upon Colloid Binding. *Phys. Rev. E* **2004**, *69*, 031903.
13. Nowak, S. A.; Chou, T. Membrane Lipid Segregation in Endocytosis. *Phys. Rev. E* **2008**, *78*, 021908.
14. Cao, S.; Wei, G.; Chen, J. Z. Y. Transformation of an Oblate-Shaped Vesicle Induced by an Adhering Spherical Particle. *Phys. Rev. E* **2011**, *84*, 050901.
15. Yi, X.; Shi, X.; Gao, H. Cellular Uptake of Elastic Nanoparticles. *Phys. Rev. Lett.* **2011**, *107*, 098101.
16. Gózdź, W. T. Deformations of Lipid Vesicles Induced by Attached Spherical Particles. *Langmuir* **2007**, *23*, 5665–5669.
17. Bahrami, A. H.; Lipowsky, R.; Weikl, T. R. Tubulation and Aggregation of Spherical Nanoparticles Adsorbed on Vesicles. *Phys. Rev. Lett.* **2012**, *109*, 188102.
18. Sarić, A.; Cacciuto, A. Mechanism of Membrane Tube Formation Induced by Adhesive Nanocomponents. *Phys. Rev. Lett.* **2012**, *109*, 188101.
19. Dasgupta, S.; Auth, T.; Gompper, G. Shape and Orientation Matter for the Cellular Uptake of Nonspherical Particles. *Nano Lett.* **2014**, *14*, 687–693.
20. Smith, K. A.; Jasnow, D.; Balazs, A. C. Designing Synthetic Vesicles that Engulf Nanoscopic Particles. *J. Chem. Phys.* **2007**, *127*, 084703.
21. Yue, T.; Zhang, X. Cooperative Effect in Receptor-Mediated Endocytosis of Multiple Nanoparticles. *ACS Nano* **2012**, *6*, 3196–3205.
22. Ding, H.; Ma, Y. Interactions between Janus Particles and Membranes. *Nanoscale* **2012**, *4*, 1116–1122.
23. Guo, R.; Mao, J.; Yan, L.-T. Unique Dynamical Approach of Fully Wrapping Dendrimer-like Soft Nanoparticles by Lipid Bilayer Membrane. *ACS Nano* **2013**, *7*, 10646–10653.
24. Salib, I.; Yong, X.; Crabb, E. J.; Moellers, N. M.; McFarlin, G. T., IV; Kuksenok, O.; Balazs, A. C. Harnessing Fluid-Driven Vesicles to Pick Up and Drop Off Janus Particles. *ACS Nano* **2013**, *7*, 1224–1238.
25. Chithrani, B. D.; Ghazani, A. A.; Chan, W. C. W. Determining the Size and Shape Dependence of Gold Nanoparticle Uptake into Mammalian Cells. *Nano Lett.* **2006**, *6*, 662–668.
26. Chithrani, B. D.; Chan, W. C. W. Elucidating the Mechanism of Cellular Uptake and Removal of Protein-Coated Gold Nanoparticles of Different Sizes and Shapes. *Nano Lett.* **2007**, *7*, 1542–1550.
27. Gao, H.; Shi, W.; Freund, L. B. Mechanics of Receptor-Mediated Endocytosis. *Proc. Natl. Acad. Sci. U.S.A.* **2005**, *102*, 9469–9474.
28. Bao, G.; Bao, X. R. Shedding Light on the Dynamics of Endocytosis and Viral Budding. *Proc. Natl. Acad. Sci. U.S.A.* **2005**, *102*, 9997–9998.
29. Decuzzi, P.; Ferrari, M. The Role of Specific and Non-Specific Interactions in Receptor-Mediated Endocytosis of Nanoparticles. *Biomaterials* **2007**, *28*, 2915–2922.
30. Zhang, S.; Li, J.; Lykotraftis, G.; Bao, G.; Suresh, S. Size-Dependent Endocytosis of Nanoparticles. *Adv. Mater.* **2009**, *21*, 419–424.
31. Schönherr, H.; Johnson, J. M.; Lenz, P.; Frank, C. W.; Boxer, S. G. Vesicle Adsorption and Lipid Bilayer Formation on Glass Studied by Atomic Force Microscopy. *Langmuir* **2004**, *20*, 11600–11606.
32. Gruhn, T.; Franke, T.; Dimova, R.; Lipowsky, R. Novel Method for Measuring the Adhesion Energy of Vesicles. *Langmuir* **2007**, *23*, 5423–5429.
33. Anderson, T. H.; Min, Y.; Weirich, K. L.; Zeng, H.; Fygenson, D.; Israelachvili, J. N. Formation of Supported Bilayers on Silica Substrates. *Langmuir* **2009**, *25*, 6997–7005.
34. Helfrich, W. Elastic Properties of Lipid Bilayers: Theory and Possible Experiments. *Z. Naturforsch., C: J. Biosci.* **1973**, *28*, 693–703.
35. Seifert, U.; Berndl, K.; Lipowsky, R. Shape Transformations of Vesicles: Phase Diagram for Spontaneous Curvature and Bilayer Coupling Model. *Phys. Rev. A* **1991**, *44*, 1182–1202.
36. Lipowsky, R. Coupling of Bending and Stretching Deformations in Vesicle Membranes. *Adv. Colloid Interface Sci.* **2014**, *208*, 14–24.
37. Fadeel, B.; Xue, D. The Ins and Outs of Phospholipid Asymmetry in the Plasma Membrane: Roles in Health and Disease. *Crit. Rev. Biochem. Mol. Biol.* **2009**, *44*, 264–77.
38. Hu, P. C.; Li, S.; Malmstadt, N. Microfluidic Fabrication of Asymmetric Giant Lipid Vesicles. *ACS Appl. Mater. Interfaces* **2011**, *3*, 1434–1440.
39. Richmond, D. L.; Schmid, E. M.; Martens, S.; Stachowiak, J. C.; Liska, N.; Fletcher, D. A. Forming Giant Vesicles with Controlled Membrane Composition, Asymmetry, and Contents. *Proc. Natl. Acad. Sci. U.S.A.* **2011**, *108*, 9431–9436.
40. Matosevic, S.; Paegel, B. M. Layer-by-Layer Cell Membrane Assembly. *Nat. Chem.* **2013**, *5*, 958–963.
41. Rózycki, B.; Lipowsky, R. Spontaneous Curvature of Bilayer Membranes from Molecular Simulations: Asymmetric Lipid Densities and Asymmetric Adsorption. *J. Chem. Phys.* **2015**, *142*, 054101.
42. Danhier, F.; Ansorena, E.; Silva, J. M.; Coco, R.; le Breton, A.; Préat, V. PLGA-Based Nanoparticles: An Overview of Biomedical Applications. *J. Controlled Release* **2012**, *161*, 505–522.
43. do Carmo, M. *Differential Geometry of Curves and Surfaces*; Prentice-Hall: Englewood Cliffs, 1976.
44. Seifert, U.; Lipowsky, R. Adhesion of Vesicles. *Phys. Rev. A* **1990**, *42*, 4768–4771.
45. Moy, V. T.; Jiao, Y.; Hillmann, T.; Lehmann, H.; Sano, T. Adhesion Energy of Receptor-Mediated Interaction Measured by Elastic Deformation. *Biophys. J.* **1999**, *76*, 1632–1638.
46. Brüning, B.-A.; Prévost, S.; Stehle, R.; Steitz, R.; Falus, P.; Farago, B.; Hellweg, T. Bilayer Undulation Dynamics in Unilamellar Phospholipid Vesicles: Effect of Temperature, Cholesterol and Trehalose. *Biochim. Biophys. Acta* **2014**, *1838*, 2412–2419.
47. Weikl, T.; Lipowsky, R. *Membrane Adhesion and Domain Formation*; Advances in Planar Lipid Bilayers and Liposomes; Elsevier, 2007; Vol. 5, pp 64–127.
48. *Structure and Dynamics of Membranes: Generic and Specific Interactions*; Lipowsky, R.; Sackmann, E., Eds.; Handbook of Biological Physics; Elsevier: Amsterdam, 1995; Vol. 1B.
49. *Biomembranes*; Shinitzky, M., Ed.; Balaban Publishers, VCH: Weinheim, 1993.
50. Dimova, R.; Aranda, S.; Bezlyepkina, N.; Nikolov, V.; Riske, K.; Lipowsky, R. A Practical Guide to Giant Vesicles. *J. Phys.: Condens. Matter* **2006**, *18*, S1151–S1176.
51. Rahimi, M.; Arroyo, M. Shape Dynamics, Lipid Hydrodynamics, and the Complex Viscoelasticity of Bilayer Membranes. *Phys. Rev. E* **2012**, *86*, 011932.
52. Fuchs, H.; Lücken, U.; Tauber, R.; Engel, A.; Geßner, R. Structural Model of Phospholipid-Reconstituted Human Transferrin Receptor Derived by Electron Microscopy. *Structure* **1998**, *6*, 1235–1243.
53. Doherty, G. J.; McMahon, H. T. Mechanics of Endocytosis. *Annu. Rev. Biochem.* **2009**, *78*, 857–902.
54. Xu, S.; Olenyuk, B. Z.; Okamoto, C. T.; Hamm-Alvarez, S. F. Targeting Receptor-Mediated Endocytotic Pathways with Nanoparticles: Rationale and Advances. *Adv. Drug Delivery Rev.* **2013**, *65*, 121–138.

55. Pearse, B.; Crowther, R. Structure and Assembly of Coated Vesicles. *Annu. Rev. Biophys. Chem.* **1987**, *16*, 49–68.
56. Loerke, D.; Mettlen, M.; Yasar, D.; Jaqaman, K.; Jaqaman, H.; Danuser, G.; Schmid, S. L. Cargo and Dynamin Regulate Clathrin-Coated Pit Maturation. *PLOS Biol.* **2009**, *7*, e1000057.
57. Cureton, D. K.; Harbison, C. E.; Parrish, C. R.; Kirchhausen, T. Limited Transferrin Receptor Clustering Allows Rapid Diffusion of Canine Parvovirus into Clathrin Endocytic Structures. *J. Virol.* **2012**, *86*, 5330–5340.
58. Vigers, G. P. A.; Crowther, R. A.; Pearse, B. M. F. Location of the 100 kDa-50 kDa Accessory Proteins in Clathrin Coats. *EMBO J.* **1986**, *5*, 2079–2085.
59. Jin, A. J.; Prasad, K.; Smith, P. D.; Lafer, E. M.; Nossal, R. Measuring the Elasticity of Clathrin-Coated Vesicles via Atomic Force Microscopy. *Biophys. J.* **2006**, *90*, 3333–3344.
60. Yersin, A.; Osada, T.; Ikai, A. Exploring Transferrin-Receptor Interactions at the Single-Molecule Level. *Biophys. J.* **2008**, *94*, 230–240.
61. Watts, C. Rapid Endocytosis of the Transferrin Receptor in the Absence of Bound Transferrin. *J. Cell Biol.* **1985**, *100*, 633–637.
62. Hopkins, C. R.; Miller, K.; Beardmore, J. M. Receptor-Mediated Endocytosis of Transferrin and Epidermal Growth Factor Receptors: A Comparison of Constitutive and Ligand-Induced Uptake. *J. Cell Sci. Suppl.* **1985**, *3*, 173–186.
63. Fourcade, B.; Miao, L.; Rao, M.; Wortis, M.; Zia, R. Scaling Analysis of Narrow Necks in Curvature Models of Fluid Lipid-Bilayer Vesicles. *Phys. Rev. E* **1994**, *49*, 5276–5286.
64. Jülicher, F.; Lipowsky, R. Shape Transformations of Inhomogeneous Vesicles with Intramembrane Domains. *Phys. Rev. E* **1996**, *53*, 2670–2683.